Journal of the Taiwan Institute of Chemical Engineers 136 (2022) 104407

Contents lists available at ScienceDirect

Journal of the Taiwan Institute of Chemical Engineers

journal homepage: www.journals.elsevier.com/journal-of-the-taiwan-institute-of-chemical-engineers

Tunable antireflective characteristics enabled by small yellow leafhopper-inspired soccer ball-shaped structure arrays

Huei-Yin Chen [a], Kuan-Ting Chiang [a], Yu-Zhe Ye [a], Kun-Yi Andrew Lin [b,*], Hongta Yang [a,*]

[a] Department of Chemical Engineering, National Chung Hsing University, 145 Xingda Road, Taichung 40227, Taiwan
[b] Department of Environmental Engineering, National Chung Hsing University, 145 Xingda Road, Taichung 40227, Taiwan

ARTICLE INFO

Keywords:
Small yellow leafhoppers
Succor ball-shaped structures
Reversible
Ambient-temperature shape memory polymers
Omnidirectional antireflection

ABSTRACT

Background: Nowadays, tunable antireflective characteristics have attracted considerable attention due to growing demands in next-generation optical energy-related fields.
Method: Bioinspired by the distinctive structural geometry on small yellow leafhopper wings, this study reports reversibly switchable antireflective characteristics enabled by ambient-temperature shape memory polymer-based soccer ball-shaped structure arrays with multilayer porous structures underneath.
Significant finds: The resulting structures behave a broadband omnidirectional antireflection performance, where the average reflectance in the visible spectrum can even be reduced by 22% for an incident angle of 75°. Interestingly, the structures can be instantaneously deformed or recovered through applying external stimuli in ambient environments. The antireflective property switches associated with the shape memory transitions deliver vast opportunities in developing smart optical devices. Moreover, the structure-shape effect and reversibility on the antireflective properties are systematically assessed in the research.

1. Introduction

In optics, incident light would reflect from discrete interfaces between two different media with a refractive index mismatch [1]. The resultant Fresnel reflection, accompanied with transmission loss, could provoke veil glare, deteriorated contrast, vision impairment, and degraded performance on optical devices and systems. Thus, a variety of vacuum-deposited antireflection coatings, consisting of single-/-multiple-layer index-matching materials with quarter-wavelength thicknesses, have been extensively employed to render mutual interferences of individual light reflections [2–6]. Unfortunately, most of the single-layer coatings are subject to impeding cost effectiveness, limited low-refractive-index material selection, and narrowband antireflection performance in a narrow range of vision. Even if the antireflective properties over the entire visible region can be realized by turning single-layer coatings to multiple-layer ones, the coatings suffer from poor mechanical properties between foreign materials, rigorous assembly precision, and cumbersome fabrication processes. While several approaches have been proposed to resolve these issues by creating low-refractive-index coatings, including a wide spectrum of nanoporous coatings created via layer-by-layer deposition of particle and oppositely charged polyelectrolyte multiple-layers, assembly of inorganic hollow particles, and phase separation of polymer blends [7–10]. A challenge still remains for accurately controlling their porosities and the corresponding refractive indices.

Over 3.8 billion years of evolution by natural selection, living creatures on earth have developed spectacular characteristics and diverse features to survive. One of the most astonishing examples is the dark-colored compound eyes of Pyralidae, commonly called snout moths [11,12]. The moth eyes are covered with hexagonally packed submicrometer-scale protuberance arrays to eliminate glare and to prevent predators from detecting their positions. Similar surface architectures are also found on transparent wings of *Greta oto* (glasswing butterfly), *Cretan cicada* (cicada cretensis), and *Orthetrum triangulare* (blue-tailed forest hawk dragonfly), giving them almost perfect camouflages without extensive coloration [13–15]. These intricate structures gradually change refractive indices over sufficient heights on surfaces, leading to less light scattering and light reflection in a wide region of wavelengths. By emulating the mother nature, a large variety of antireflective structures, such as dome-shaped structures, conical structures, nipple-shaped structures, and pyramid-like structures, are designed and developed through lithography-based fabrication

* Corresponding authors.
E-mail addresses: linky@nchu.edu.tw (K.-Y.A. Lin), hyang@dragon.nchu.edu.tw (H. Yang).

https://doi.org/10.1016/j.jtice.2022.104407
Received 27 February 2022; Received in revised form 25 May 2022; Accepted 2 June 2022
Available online 16 June 2022

methodologies to suppresses visible light reflection in the past decade [16–19]. Nevertheless, the most common methodologies, including photolithography, interference lithography, nanoimprint lithography, and electron beam lithography, require dedicate equipment and sophisticate fabrication processes [20–23]. Accordingly, numerous relatively straightforward and inexpensive colloidal self-assembly methodologies have been exploited to render an alternative in creating such antireflective structures [24–26]. Nevertheless, the structures, templated from self-assembled colloids, are limited by insufficient structural heights. The resulting shape refractive index transitions cannot effectively suppress the light reflection at large incidence angles.

Recently, a new class of natural antireflective architectures has been discovered on *Thaia rubiginosa* (the small yellow leafhopper) wings [27,28]. After molting, the leafhoppers release and anoint a proteinaceous brochosome-containing secretion across their wings to camouflage themselves, and to protect their egg chambers. The distributed secretory brochosomes are in the form of hollow submicrometer-scale granules with nanometer-scale indentations, resulting in a structural geometry similar to a soccer ball. The peculiar geometry greatly moderates the refractive index changes over wide angle of incidence, leading to omnidirectional antireflective behaviors and a nearly invisible appearance. However, there remains an enormous challenge to create such complex structures by employing current micro/nanomanufacturing technologies. To confront the challenge, artificial brochosomes had been fabricated through electrochemical deposition of either metals or metal oxides onto hierarchical double-layer colloidal crystal templates, followed by a wet etching procedure to eliminate the templates [29–31]. While the artificial brochosome-covered substrates exhibit ultra-antireflection performances, the micrometer-scale metal-based hollow structures indubitably result in enhanced visible light scattering and impaired optical transparency.

Nowadays, tunable antireflective characteristics have attracted considerable attention due to growing demands in flexible solar cells, architectural partitions, smart displays, rewritable/reconfigurable optical devices, and next-generation optical energy-related fields [32,33]. Stimuli-responsive shape memory polymers, which can gradually and reversibly transit between a permanent state and a temporary state in responding to diverse external stimuli, may hold a key to create deformable antireflective structures and thence reverse their corresponding antireflective characteristics [34,35]. In sharp contrast to elastic polymeric materials (e.g., hydrogels and elastomers), the shape memory polymers are capable of retaining their temporaily deformed configurations even after relieving the external stimuli. Among diversed shape memory polymers, thermoresponsive ones, whose shape memory cycles are triggered by either heating or energy absorption, are mostly utilized in fabricating reconfigurable structures [36,37]. Upon heating through their glass-transition ranges, the macromolecular chains are configurable in rubbery states, while the chains turn brittle and rigid in glassy states upon cooling. Nevertheless, most heat-demanding shape alternations are restricted to slow response speeds and long recovery periods due to their low heat transfer coefficients, and therefore impede their applications in integrated active devices.

With the progressive invention of shape memory polymers, rapid shape memory cycles triggered by solvent-evaporation-stimulated capillary forces under ambient conditions have been actualized to overcome the knotty shortcomings of thermoresponsive shape memory polymers [38–40]. The macromolecular chain configurations can be alternated between a permanent state and a temporary state through drying out of household solvents with required surface tensions at room temperature. Undoubtedly, integration of bioinspired structures and the room-temperature shape memory polymers creates vast opportunities in developing deformable structures, thereby gaining intelligent switchable functionalities. Herein, room-temperature shape memory polymer-based soccer ball-shaped structure arrays, bioinspired by the small yellow leafhopper-released brochosomes, are engineered through a non-lithography-based fabrication approach. In our previous work, artificial brochosomes have been created to serve as antireflective structures [41]. Nevertheless, the antireflection performance was not significantly improved, arising from the refractive index mismatch at the structure/substrate interface. To address the issue, multilayered porous structures are self-assembled beneath the artificial brochosomes to further moderate the refractive index transition in this study. The resulting broadband omnidirectional antireflective characteristics associated with the reversible shape memory transitions enable a wealth of novel optical applications.

2. Experimental section

Reagents and Specimens. The reagents used for a typical Stöber silica colloid synthesis, consisting of tetraethyl orthosilicate, anhydrous ethanol, and ammonium hydroxide solution (28 wt.%), are purchased from Merck & Company, Incorporated [42]. 2,2,3,3,3-Pentafluoropropyl acrylate (PFPA) monomer, ethoxylated trimethylolpropane triacrylate (ETPTA) monomer, ethylene glycol diacrylate (EGDA) monomer, and the photo-initiator, 2-hydroxy-2-methyl-1-phenyl-1-propanone (HMPPP), are provided by Sartomer Company Corporation, and BASF Corporation, respectively. Aqueous hydrofluoric acid (48 wt.%) is obtained from Merck & Company, Incorporated. All of the reagents are used directly without any purification. Optical polyethylene terephthalate (PET) film acquired from Resound Technology Company, Incorporated are rinsed with anhydrous ethanol before use. The small yellow leafhopper specimens are purchased from The Muhsheng Insect Museum (Nantou, Taiwan), and analyzed as received.

Self-Assembly of Two-Dimensional Close-Packed Hole Arrays. Spherical 450 nm StÖber silica colloids are dispersed in a mixture of PFPA monomer and HMPPP (0.5 vol.%). After eliminating any aggregate through a syringe filtration process, the suspension is continuously dropped on water, during which the silica colloids are assembled into a two-dimensional hexagonal close-packed arrangement spontaneously. An optical PET film immersed in the water is then pulled upward at a constant speed of 0.5 mm/sec using a syringe pump, meanwhile, the floating PFPA monomer-covered silica colloidal crystals are transferred onto the PET film. During the modified Langmuir-Blodgett self-assembly process, the voids between the silica colloids and the film are rapidly filled by the liquiform PFPA monomers. After photo-polymerization of the monomers in an OPAS XLite™ 500 UV curing chamber, the embedded silica colloidal crystals can be removed by diluted aqueous hydrofluoric acid (2 wt.%) to bring out a two-dimensional close-packed 450 nm poly(PFPA) hole array.

Templating Fabrication of Close-Packed Soccer Ball-Shaped Structure Arrays. Self-assembled monolayer 90 nm StÖber silica colloidal crystals, covered with a ETPTA monomer/HMPPP (0.5 vol.%) mixture, is transferred onto the close-packed 450 nm poly(PFPA) hole arrays. The silica colloids are temporarily attached to the holes after photo-polymerizing the ETPTA/EGDA monomers. The modified Langmuir-Blodgett deposition procedure can be performed for multiple times to deposit multilayer 90 nm silica colloidal crystals in demand. An ETPTA monomer (24.5 vol.%)/EGDA monomer (75 vol.%)/HMPPP (0.5 vol.%) mixture is then casted onto the multilayer silica colloidal crystal-coated holes, followed by a degassing process (10 min) to eliminate trapped air. After another photo-polymerization procedure, the silica colloid/poly(ETPTA)/poly(EGDA) composite can be stripped from the poly(PFPA) holes. Lastly, the embedded 90 nm silica colloids are eliminated using ethanol-based hydrofluoric acid (2 wt.%) to afford a close-packed soccer ball-shaped structure array.

Characterizations. Appearances and surface morphologies of the samples are characterized with a Sony ZV-1 digital camera and a LEO 1530 field-emission scanning electron microscope (FE-SEM), respectively. Uniform platinum films are sputter-coated onto the samples prior to SEM imaging. Reflectance and transmittance spectra from 380 to 800 nm are carried out using an Ocean Optics HR4000 ultraviolet-visible

spectrometer with a halogen-tungsten power source.

3. Results and discussion

The small yellow leafhopper wings are with low haze and high transparency under ambient environments, providing them nearly perfect camouflage against avian predators (Fig. 1(a)). Their wings only reflect under 3% of ambient light (black solid curve), and exhibit an average transmittance of 96% (black dashed curve) in the visible spectrum (Fig. 1(b)). The high optical transparency is achieved with the van der Waals stacking of proteinaceous brochosomes (Fig. 1(c) and (d)), producing intracellularly inside the Malpighian tubules. These integumental brochosomes are submicrometer-scale granules (~450 nm) with nanometer-scale indentations (~90 nm) arranged in an intricate three-dimensional periodicity, making their structural geometries similar to a soccer ball. Interestingly, after scrubbing the non-sticky brochosome coating, the average reflectance is increased by 5%, while the average transmittance is decreased by 5% (Fig. 1(b)). The findings indicate that the soccer ball-shaped granules build a refractive index gradient to eliminate light reflection rather than to absorb the incident light.

Bioinspired by the structural geometry of small yellow leafhopper-secreted brochosomes, close-packed soccer ball-shaped structure arrays with multilayer porous structures underneath (SBSSA-MPSU) are engineered in this study (Fig. 2). Firstly, monolayer PFPA monomer-covered silica colloids with diameters of 450 nm are assembled into a close-packed arrangement and then transferred onto a PET film in a modified Langmuir-Blodgett process. The self-assembly is derived by surface tension difference between water and the monomer. On account of gravity and capillary forces, the liquiform PFPA monomers spontaneously fill the space between the colloidal crystals and the film. After polymerization of PFPA monomers on exposure to ultraviolet radiation, the embedded colloids are wet-etched to bring out a hexagonally close-packed poly(PFPA) hole array (Fig. S1). It is evident that the holes with varied openings can be fabricated through using silica colloidal suspensions with different colloid volume fractions. Moreover, hemispherical holes with an average opening size of 450 nm are generated as the colloid volume fraction of applied silica colloid suspension reaches 35 vol.%. Subsequently, the hemispherical hole array is coated with demanded multilayer 90 nm silica colloid crystals by repeating the as-developed Langmuir-Blodgett process, in which the monomers serve as adhesives to retain the structural integrity (Fig. S2). Afterwards, an ETPTA monomer/EGDA monomer/HMPPP mixture with a proper amount is gently casted on the multilayer silica colloidal crystal-coated hole array, and then infiltrate onto the holes in a degassing process. After exposure to ultraviolet radiation, a hemispherical silica colloid/poly (ETPTA)/poly(EGDA) structure array can be easily stripped from the template, benefiting from the low surface energy of poly(PFPA) (Fig. S3). Even though several blemishes are noticed, close-packed raspberry-shaped 450 nm structures with the embedding of tens of 90 nm silica colloids are well retained through the templating procedure. It is worth noting that the air trapped in the holes is not completely eliminated, leading to the formation of partially embedded silica colloids in the upper region of the raspberry-shaped structures. Lastly, the silica colloids are wet-etched to engineer the soccer ball-shaped structures.

It is found that the resulting hemispherical structures, with an average height of 225 nm and an average width of 450 nm, are periodically arranged in a hexagonal ordering on the substrate (Fig. 3). Compared with the bump-shaped structures templated from an uncovered poly(PFPA) hole array (Fig. 3(a) and (b)), soccer ball-shaped structures with 90 nm pores are engineered through applying

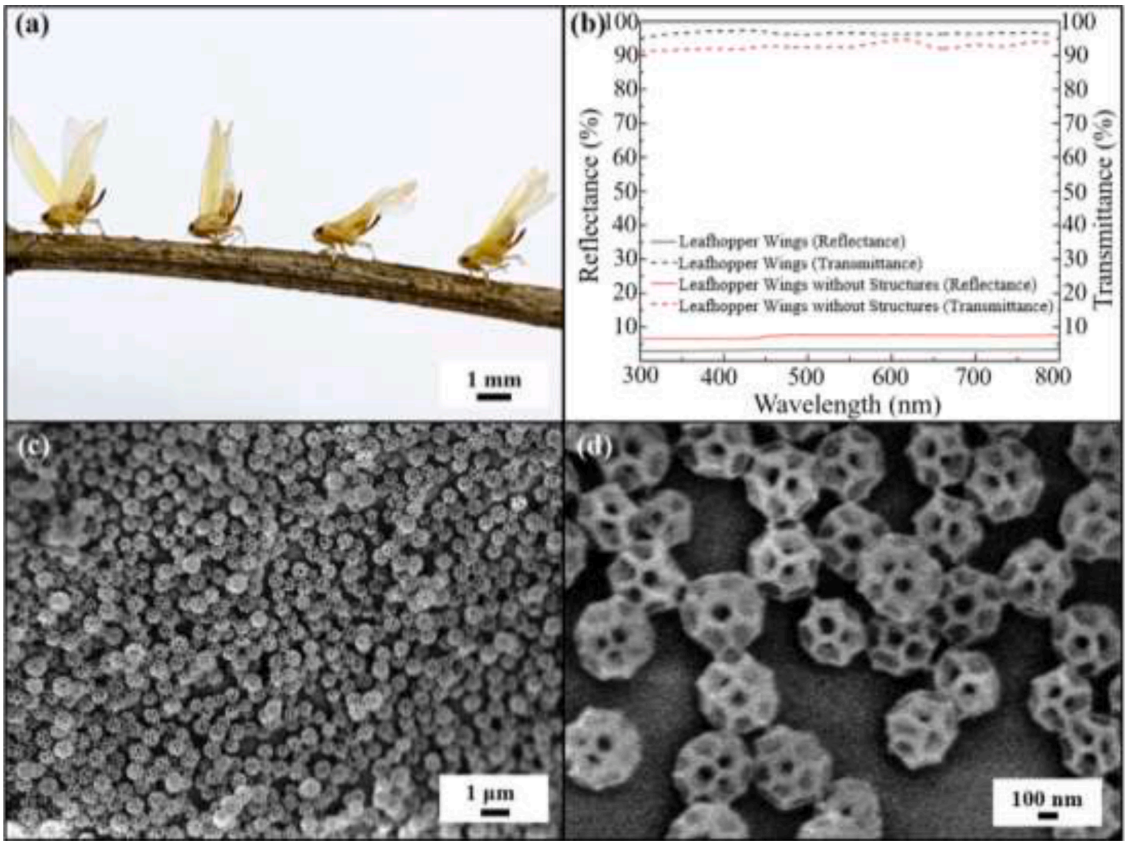

Fig. 1. (a) Picture of small yellow leafhoppers (*Thaia rubiginosa*) photographed under white light illumination. (b) Comparison of normal-incidence specular reflectances and normal-incidence specular transmittances acquired from brochosome-covered leafhopper wings (black) and bare leafhopper wings (red). (c) SEM image of the brochosomes on the leafhopper wings. (d) Magnified SEM image of (c).

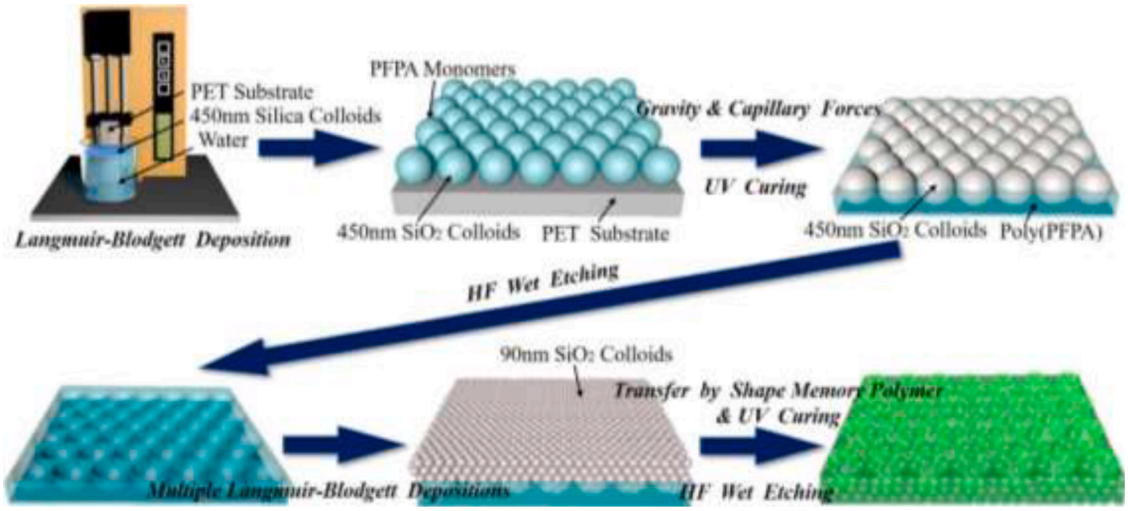

Fig. 2. Schematic of the templating procedures for fabricating soccer ball-shaped structure arrays with multilayer porous structures underneath.

multilayer silica colloidal crystal-coated poly(PFPA) hole arrays as templates (Fig. 3 (c-h)). The thickness of porous structures is determined by depositing varied layers of silica colloidal crystals onto the holes. From the magnified cross-sectional views, it is clearly evident that a soccer ball-shaped structure array (SBSSA), a soccer ball-shaped structure array with single-layer of porous structures underneath (SBSSA-1PSU), and a soccer ball-shaped structure array with triple-layer of porous structures underneath (SBSSA-3PSU) can be templated from double-layer silica colloidal crystal-coated holes, triple-layer silica colloidal crystal-coated holes, and penta-layer silica colloidal crystal-coated holes, respectively.

To investigate the small yellow leafhopper-inspired antireflective structure arrays, normal-incidence specular reflectances, transmittances, and absorbances of the samples are collected and compared. As shown in Fig. S4, all the samples are with similar absorbances (ca. 2%). Besides that, a featureless poly(ETPTA)/poly(EGDA) substrate (black curves) behaves an average reflectance of 10% and an average transmittance of 88% across the entire visible spectrum (Fig. 4(a) and (b)), which are attributable to an abrupt change in refractive index on the surface. The refractive index change can be moderated by introducing submicrometer-scale structure arrays to suppress the light reflection. Unexpectedly, even though the bump array-covered substrate (blue curves) displays a lower average reflectance, the corresponding average transmittance is only slightly increased. The unreformed transmittance is ascribed to light refraction and light scattering from the submicrometer-scale bumps. Comparatively, the antireflection performance is obviously improved by applying the SBSSA (orange curves); especially, the specular reflectance of the SBSSA-covered substrate is reduced by 5%, and its corresponding specular transmittance is raised by 5%. It is evident that the unfavorable optical impairments can be diminished by creating nanometer-scale pores within the structures. Importantly, the broadband antireflection capability can be further enhanced through designing and developing multilayer porous structures underneath the soccer ball-shaped structures (green curves and red curves). Thicker porous structures possess smoother porosity changes and effective refractive index transitions across the templated structures (Fig. 4(c)), and therefore are capable of suppressing optical reflection more efficiently (Figs. S5 and 4 (d)). It is found that the average reflectance of the SBSSA-3PSU-covered substrate reaches less than 3%, while an average transmittance of 96% can be achieved. To better comprehend the effect of porous structure thickness on the antireflective properties, average transmittances of the SBSSA-MPSU-covered substrates in the visible spectrum are acquired (Fig. S6). In fact, the porous structures function as a single-layer antireflection coating. Accordingly, the optimum thickness of the coating equals to a quarter of visible wavelength. As a result, the average transmittance is increased with the number of porous structure layers, whereas the average transmittance remains unchanged as the porous structures with triple-layers or more are generated underneath the SBSSAs. The results reveal that optimized antireflective structure arrays can be realized through modifying the thickness of porous structures to suppress overall optical reflection.

To further assess their omnidirectional antireflection capabilities, specular reflectances and specular transmittances of the aforementioned structure array-covered substrates are collected at varied incident angles of 15°, 30°, 45°, 60° to 75° (Fig. S7). The corresponding average reflectances and transmittances in the visible spectrum are computed and compared in Fig. 5. All the average reflectances increase as the incident angle varies from 0° to 75°, whereas the average transmittances present opposite tendencies. Importantly, the antireflective characteristics of the structures with thicker porous structures are less sensitive to the angle of incident light. In comparison to the optical properties of a bare substrate (black curves), the average reflectance of the SBSSA-3PSU-covered substrate is reduced by 22% for an incident angle of 75°, while the average transmittance of that can still maintain 87% (red curves). The low reflectivity and high transparency in the wide range of incident angles are even competitive with the optical performance of the small yellow leafhopper wings (Fig. S8). Besides that, the insert in Fig. 5(b) once more demonstrates its omnidirectional antireflection capability. In contrast to the appearance of a bare substrate (the left one), the SBSSA-3PSU-covered substrate (the right one) taken at 75° is highly transparent under natural lighting. The results further disclose that the SBSSA-MPSU generate moderate effective refractive index gradients not only at normal-incidence, but also for wide angles of incidence.

Benefiting from the low glass transition temperature (−42 °C) of poly (ETPTA)/poly(EGDA) copolymer, its shape changing of the as-fabricated SBSSA-3PSU can be triggered by applying external stimuli at ambient temperature [43,44]. As displayed in Fig. 6(a), the structures are temporarily collapsed after rinsing the substrate with water, followed by evaporating the water imbibed in the macropores under ambient conditions. The high water-evaporation-stimulated capillary pressure is capable of overcoming the Young's modulus of the water-swollen copolymer, and therefore distorting the shape of the templated structures within 1 min [45–48]. After complete evaporation, the van der Waals interactions between the stressed copolymer chains can stabilize the deformed structures, which can be retained for more than 6 months. Interestingly, similar capillary pressures induced by low-surface-tension solvents such as ethanol can active the recovery of their memorized permanent shape in a few seconds under ambient conditions (Fig. 6(b)). The rapid diffusion of employed solvent molecules within the copolymer weakens the van der Waals attractions

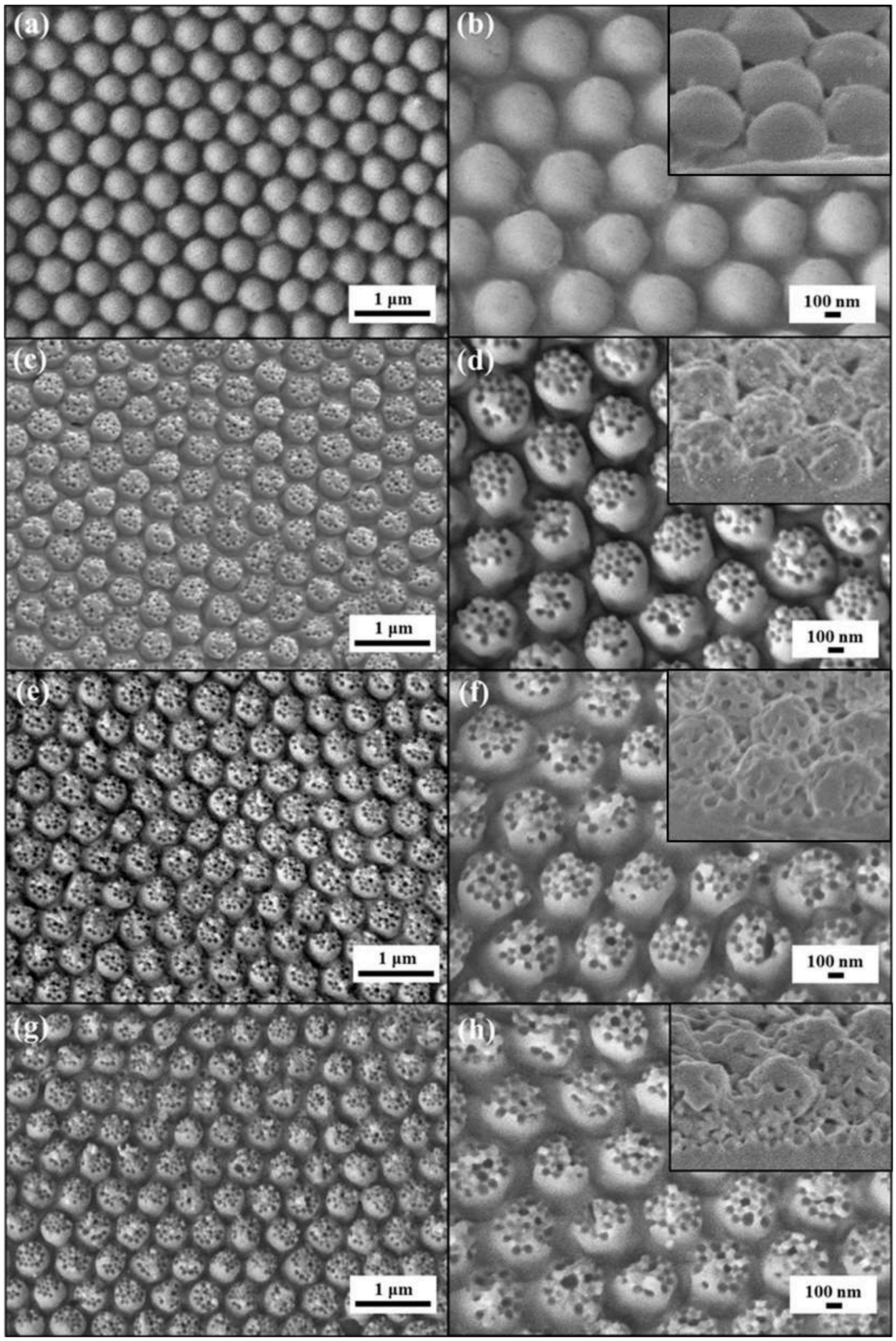

Fig. 3. (a) Top-view SEM image of hexagonal close-packed 450 nm bump arrays. (b) Magnified SEM image of (a). Top-view SEM images of hexagonal close-packed 450 nm soccer ball-shaped structure arrays templated from (c), (d) double-layer of 90 nm silica colloidal crystals, (e), (f) triple-layer of 90 nm silica colloidal crystals, and (g), (h) penta-layer of 90 nm silica colloidal crystals. The images in (d), (f), and (h) are magnified top-view SEM images of (c), (e), and (g), respectively. The inserts displaying the corresponding side-view SEM images.

between the copolymer chains and relaxes the copolymer network [49]. The resulting swelling expands the deformed structures and subsequently triggers their shape recovery. Critically, the Young's modulus of the copolymer surpasses the low solvent-evaporation-stimulated capillary pressure, indicating that the recovered structures have the ability to maintain their permanent shape during air-drying. The ambient-temperature shape memory characteristics provide a platform to easily transform the broadband antireflection performance, which is associated with the structural transition of the SBSSA-3PSU (Fig. 6(c) and (d)). Apparently, the sharper porosity and effective refractive index changes (Fig. S9), originated from the squeezed structures, resulting in increased average reflectances and decreased average transmittances at varied angles of incidence (blue curves). By contrast, the average reflectances and transmittances of the recovered structures (orange curves) match reasonably well with those of the original structures (red curves), confirming the reappearance of broadband antireflective properties. In addition, the results further indicate that the deformed structures and the corresponding effective refractive index change can be fully recovered. The switchable antireflective properties, enabled by drying out of demanded solvents, can be repeated for more than 100 deforming/recovering cycles (Fig. 6(e)). Compared with the appearance of the deformed SBSSA-3PSU-covered substrate (left half), the recovered SBSSA-3PSU-covered substrate (right half) exhibits the relatively high optical transparency (Fig. 6(f)). The findings further disclose that the

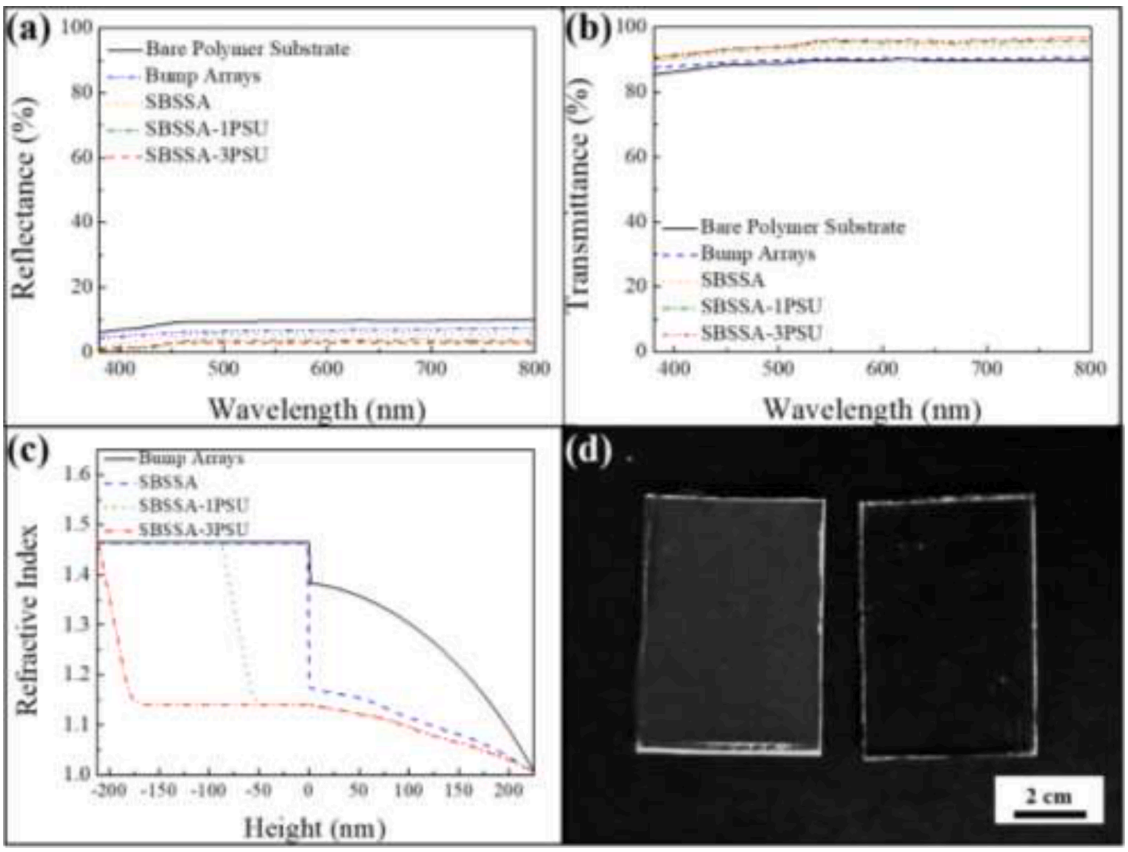

Fig. 4. Comparison of (a) normal-incidence specular reflectances and (b) normal-incidence specular transmittances acquired from a bare polymer substrate (black) and polymer substrates coated with 450 nm bump arrays (blue), soccer ball-shaped 450 nm structure arrays (orange), soccer ball-shaped 450 nm structure arrays with single-layer of porous structures underneath (green), and soccer ball-shaped 450 nm structure arrays with triple-layer of porous structures underneath (red). (c) Comparison of computed effective refractive index profiles of the structures. (d) Picture of a bare polymer substrate (the left one) and a polymer substrate coated with soccer ball-shaped 450 nm structure arrays with triple-layer of porous structures underneath (the right one) photographed under white light illumination.

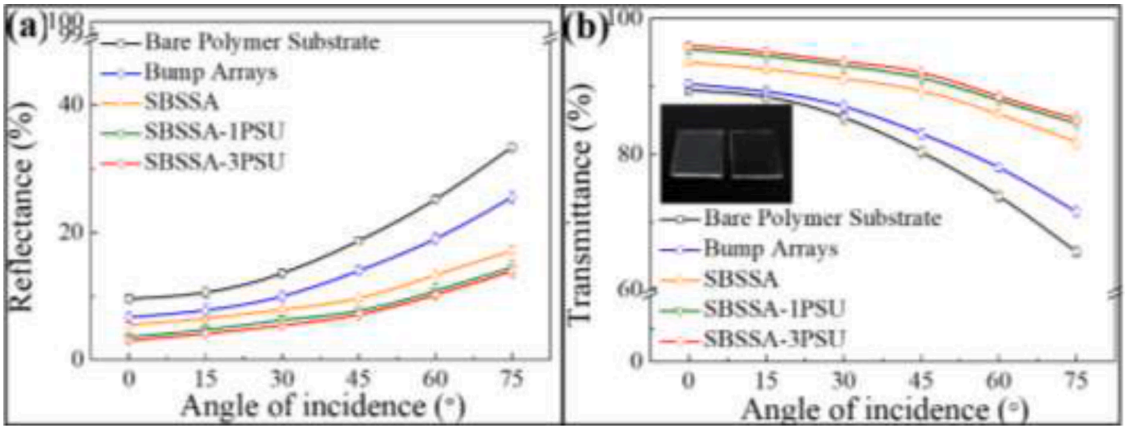

Fig. 5. Comparison of (a) average reflectances and (b) average transmittances in the visible spectrum acquired from a bare polymer substrate (black) and polymer substrates coated with 450 nm bump arrays (blue), soccer ball-shaped 450 nm structure arrays (orange), soccer ball-shaped 450 nm structure arrays with single-layer of porous structures underneath (green), and soccer ball-shaped 450 nm structure arrays with triple-layer of porous structures underneath (red) at varied angles of incidence. The insert displaying photographic images of a bare polymer substrate (the left one) and a polymer substrate coated with soccer ball-shaped 450 nm structure arrays with triple-layer of porous structures underneath (the right one) taken at 75°

shape memory polymer-based antireflective structures are well-preserved in the shape memory cycles.

More interestingly, the antireflection capability can be accurately adjusted right after applying appropriate contact pressures. In this study, external contact pressures of 0.5 N/cm^2, 1.0 N/cm^2, 1.5 N/cm^2, and 2.0 N/cm^2 are exerted on the temporarily deformed SBSSA-3PSUs, respectively, through placing demanded calibration weights on the substrate. The substrate is covered with a glass coverslip to ensure that the contact pressure is imposed evenly on the structures. Afterwards, the calibration weights are vertically uplifted, during which van der Waals interactions are generated between the glass coverslip and the structures to restore their original shape. It is worth noting that insufficient

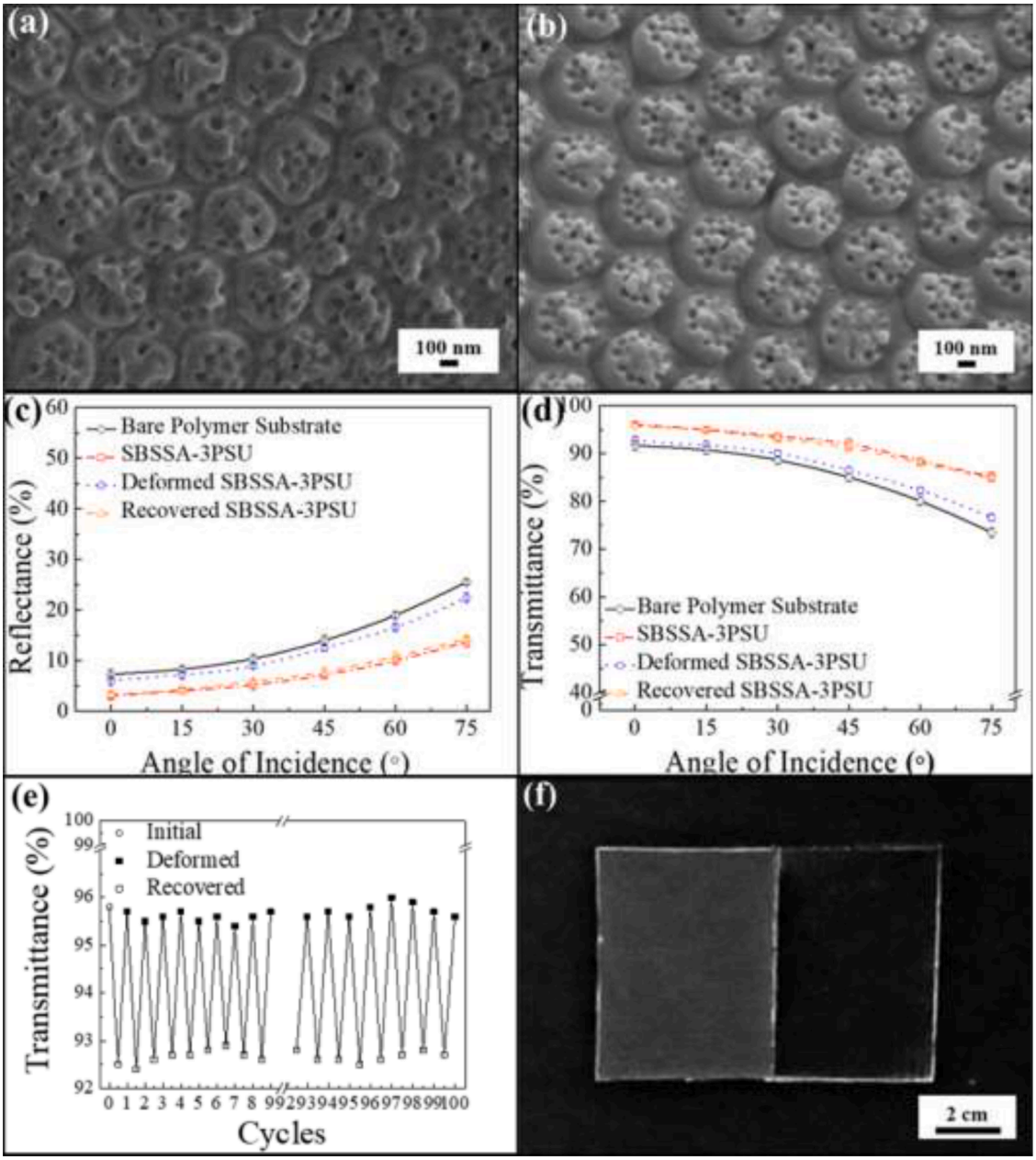

Fig. 6. Top-view SEM images of (a) deformed and (b) recovered soccer ball-shaped 450 nm structure arrays with triple-layer of porous structures underneath. Comparison of (c) average reflectances and (d) average transmittances in the visible spectrum acquired from a bare polymer substrate (black), and a polymer substrate coated with soccer ball-shaped 450 nm structure arrays with triple-layer of porous structures underneath in its original state (red), deformed state (blue), and recovered state (orange), triggered by ethanol drying, at varied angles of incidence. (e) Switchable antireflective characteristics of the as-engineered coating enabled by an ethanol drying procedure. (f) Picture of a polymer substrate coated with deformed antireflective structures arrays (the left half) and recovered antireflective structures (right half) after 100 deforming/recovering cycles.

attractive forces can only allow the deformed structures to be recovered partially, while the SBSSA-3PSU can be fully recovered as a contact pressure of 2.0 N/cm^2 is applied (Fig. S10). The observed partial recovery of the templated antireflective structures results in a varied degree of antireflection capability (Fig. 7(a) and (b)). Evidently, further recoveries of demanded structures, triggered by applying higher contact pressures, leads to the improved antireflection performances. The average reflectances and transmittances of the fully-recovered SBSSA-3PSU-covered substrate (green curves) match those of the undamaged SBSSA-3PSU-covered substrate (red curves), revealing that the broadband (visible) antireflective characteristics are fully restored. As mentioned earlier, the recovered antireflective structures can once again be deformed through drying out of water at ambient temperature. The corresponding contact pressure-induced antireflection performance can therefore be reversibly switched (Fig. 7(c) and (d)).

4. Conclusions

In summary, stimuli-responsive soccer ball-shaped structure arrays with multilayer porous structures underneath, bioinspired by brochosomes on small yellow leafhopper wings, are engineered through combining a self-assembly technology with an ambient-temperature shape memory polymer. The resulting structures generate moderate effective refractive index gradients for wide angles of incidence, leading to a broadband omnidirectional antireflection performance. Benefiting from their low glass transition temperature, the shape memory polymer-

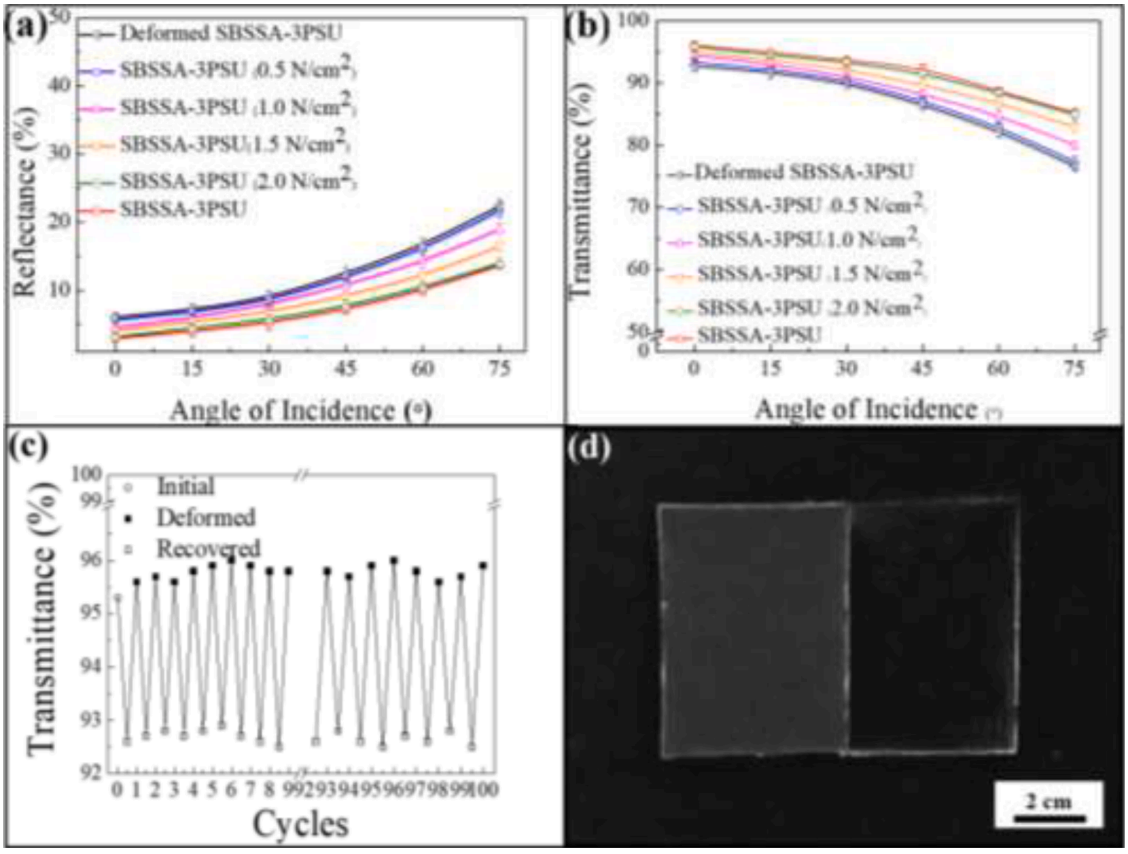

Fig. 7. Comparison of (a) average reflectances and (b) average transmittances in the visible spectrum acquired from a polymer substrate coated with deformed soccer ball-shaped 450 nm structure arrays with triple-layer of porous structures underneath after applying varied contact pressures, 0.5 N/cm^2 (blue), 1.0 N/cm^2 (pink), 1.5 N/cm^2 (orange), and 2.0 N/cm^2 (green), at varied angles of incidence. (c) Switchable antireflective characteristics of the as-engineered coating enabled by applying contact pressures. (d) Picture of a polymer substrate coated with deformed antireflective structures arrays (the left half) and recovered antireflective structures (right half) after 100 deforming/recovering cycles.

based structures can be temporally deformed and recovered through either drying out of appropriate solvents or applying external contact pressures in ambient environments. As a result, the corresponding antireflection performances are therefore switched as demanded. In addition, it is well demonstrated that the structure deforming/recovering transitions can be repeated for more than 100 cycles. The reversibly switchable antireflective structures could find a wide range of technological applications as camera lenses, holograms, displays, and flexible screens.

Declaration of Competing Interest

The authors declare that they have no known competing financial interests or personal relationships that could have appeared to influence the work reported in this paper.

Acknowledgments

This study is supported by the Ministry of Science and Technology (Grant Nos. MOST 108–2221-E-005–038-MY2, MOST 109–2221-E-005–018, and MOST 110–2221-E-005–050-MY2). The acknowledgement is made to the Instrument Center of National Chung Hsing University for the use of Field Emission Scanning Electron Microscope.

Supplementary materials

Supplementary material associated with this article can be found, in the online version, at doi:10.1016/j.jtice.2022.104407.

References

[1] Shan XC, Wang F, Wang DJ, Wen SH, Chen CH, Di XJ, Nie P, Liao JY, Liu YT, Ding L, Reece PJ, Jin DY. Optical tweezers beyond refractive index mismatch using highly doped upconversion nanoparticles. Nat Nanotechnol 2021;16(5):531–7.
[2] Damgaard-Carstensen C, Thomaschewski M, Ding F, Bozhevolnyi SI. Electrical tuning of fresnel lens in reflection. ACS Photonics 2021;8(6):1576–81.
[3] Pfeiffer K, Ghazaryan L, Schulz U, Szeghalmi A. Wide-angle broadband antireflection coatings prepared by atomic layer deposition. ACS Appl Mater Interfaces 2019;11(24):21887–94.
[4] Pecora EF, Cordaro A, Kik PG, Brongersma ML. Broadband antireflection coatings employing multiresonant dielectric metasurfaces. ACS Photonics 2018;5(11):4456–62.
[5] Chi FT, ZengYY LC, Pan N, Ding CC, Yi FC. Highly stable self-cleaning antireflection coatings from fluoropolymer brush grafted silica nanoparticles. Appl Surf Sci 2020;507:144836.
[6] Bacon-Brown DA, Braun PV. Tunable antireflection coating to remove index-matching requirement for interference lithography. Adv Opt Mater 2018;6(8):1701049.
[7] Yang PP, Li Z, Gao ZZ, Song MQ, Zhou JY, Fang QR, Xue M, Qiu SL. Solvent-free crystallization of zeolitic imidazolate framework membrane via layer-by-layer deposition. ACS Sustain Chem Eng 2019;7(4):4158–64.
[8] Jung A, Ha N, Kim N, Oh J, Son JG, Lim HK, Yeom B. Multiple transfer of layer-by-layer nanofunctional films by adhesion controls. ACS Appl Mater Interfaces 2019;11(51):48476–86.
[9] Lin TX, Chen KJ, Chen PY, Jan JS. Broadband antireflection coatings based on low surface energy/refractive index silica/fluorinated polymer nanocomposites. ACS Appl Nano Mater 2018;1(2):741–50.
[10] Syurik J, Jacucci G, Onelli OD, Holscher H, Vignolini S. Bio-inspired highly scattering networks via polymer phase separation. Adv Funct Mater 2018;28(24):1706901.
[11] Wang WJ, Li J, Li RH, Li BQ, Mei XS, Sun XF. Fabrication of hierarchical micro/nano compound eyes. ACS Appl Mater Interfaces 2019;11(37):34507–16.
[12] Cao JJ, Hou ZS, Tian ZN, Hua JG, Zhang YL, Chen QD. Bioinspired zoom compound eyes enable variable-focus imaging. ACS Appl Mater Interfaces 2020;12(9):10107–17.

[13] Liu XH, Cheng HY, Guo ZZ, Zhan Q, Qian JW, Wang XB. Bifunctional moth-eye-like nanostructured black titania nanocomposites for solar-driven clean water generation. ACS Appl Mater Interfaces 2018;10(46):39661–9.
[14] Wang S, Dai JN, Hu JH, Zhang S, Xu LL, Long HL, Chen JW, Wan QX, Kuo HC, Chen CQ. Ultrahigh degree of optical polarization above 80% in algan-based deep-ultraviolet led with moth-eye microstructure. ACS Photonics 2018;5(9):3534–40.
[15] Narasimhan V, Siddique RH, Lee JO, Kumar S, Ndjamen B, Du J, Hong N, Sretavan D, Choo H. Multifunctional biophotonic nanostructures inspired by the longtail glasswing butterfly for medical devices. Nat Nanotechnol 2018;13(6):512–9.
[16] Kovacic M, Will PA, Lipovsek B, Topic M, Lenk S, Reineke S, Krc J. Coupled optical modeling for optimization of organic light-emitting diodes with external outcoupling structures. ACS Photonics 2018;5(2):422–30.
[17] Sim YH, Yun MJ, Cha SI, Seo SH, Lee DY. Improvement in energy conversion efficiency by modification of photon distribution within the photoanode of dye-sensitized solar cells. ACS Omega 2018;3(1):698–705.
[18] Xie ZH, Stoesser T. Two-phase flow simulation of breaking solitary waves over surface-piercing and submerged conical structures. Ocean Eng 2020;213:107679.
[19] Wu T, Wang GC, Li J, Yan K. Investigation on gear rolling process using conical gear rollers and design method of the conical gear roller. J Mater Process Technol 2018;259:141–9.
[20] Liu WF, Wang JB, Xu XZ, Zhao CZ, Xu XB, Weiss PS. Single-step dual-layer photolithography for tunable and scalable nanopatterning. ACS Nano 2021;15(7):12180–8.
[21] Kaholi F, Ghazyani N, Riahi M, Zare-Behtash H, Ara MH, Heydari E. Upconverting nanoengineered surfaces: maskless photolithography for security applications. ACS Appl Nano Mater 2019;2(6):3590–6.
[22] Bhingardive V, Menahem L, Schvartzman M. Soft thermal nanoimprint lithography using a nanocomposite mold. Nano Res 2018;11(5):2705–14.
[23] Zhang X, Xu YR, Zhang WW, Fu XX, Hao ZB, He MJ, Trefilov D, Ning XH, Ge HX, Chen YF. Controllable subtractive nanoimprint lithography for precisely fabricating paclitaxel-loaded plga nanocylinders to enhance anticancer efficacy. ACS Appl Mater Interfaces 2020;12(13):14797–805.
[24] Song YY, Sun JB, Sun M, Simalou O, Gao HQ, Peng J, Shu YH, Zhai L, Lu R. Multi-stimuli-responsive fluorescent materials based on n, o-chelated bf2 complexes: self-assembling, sensory properties and detection of latent fingerprint. Opt Mater 2021;115:111006.
[25] Nunez CG, Navaraj WT, Liu FY, Shakthivel D, Dahiya R. Large-area self-assembly of silica microspheres/nanospheres by temperature-assisted dip-coating. ACS Appl Mater Interfaces 2018;10(3):3058–68.
[26] Peng J, Zhai F, Guo XY, Jiang XP, Ma YG. Self-assembly and phase separation of amphiphilic dyads based on 4,7-bis(2-thienyl) benzothiodiazole and perylene diimide. RSC Adv 2014;4(25):13078–84.
[27] Rakitov R, Gorb SN. Brochosomes protect leafhoppers (insecta, hemiptera, cicadellidae) from sticky exudates. J R Soc Interfaces 2013;10(87):5.
[28] Watson GS, Watson JA, Cribb BW. Diversity of cuticular micro- and nanostructures on insects: properties, functions, and potential applications. Annu Rev Entomol 2017;62:185–205.
[29] Yang SK, Sun N, Stogin BB, Wang J, Huang Y, Wong TS. Ultra-antireflective synthetic brochosomes. Nat Commun 2017;8:1285.
[30] Ding QQ, Kang YL, Li WL, Sun GF, Liu H, Li M, Ye ZR, Zhou M, Zhou JG, Yang SK. Bioinspired brochosomes as broadband and omnidirectional surface-enhanced raman scattering substrates. J Phys Chem Lett 2019;10(21):6484–91.
[31] Pan Q, Zhang HF, Yang YP, Cheng CW. 3D brochosomes-like $TiO_2/WO_3/BiVO_4$ arrays as photoanode for photoelectrochemical hydrogen production. Small 2019;15(28):1900924.
[32] Lin HF, Qiu ZY, Huang PNA, Zeng LL, Liang YF, Zeng CH, Lin RX, Yuan MY, Hong RJ. Preparation of antireflective coatings with moisture resistance and a widely tunable refractive index by combining the sol-gel method with evaporation concentration. Constr Build Mater 2022;318:125810.
[33] Gregorcic P. Comment on "bioinspired reversible switch between underwater superoleophobicity/superaerophobicity and oleophilicity/uaerophilicity and improved antireflective property on the nanosecond laser-ablated superhydrophobic titanium surfaces". ACS Appl Mater Interfaces 2021;13(2):2117–27.
[34] Huang YN, Fan LF, Rong MZ, Zhang MQ, Gao YM. External stress-free reversible multiple shape memory polymers. ACS Appl Mater Interfaces 2019;11(34):31346–55.
[35] Kabir MH, Hazama T, Watanabe Y, Gong J, Murase K, Sunada T, Furukawa H. Smart hydrogel with shape memory for biomedical applications. J Taiwan Inst Chem Eng 2014;45(6):3134–8.
[36] Maiti B, Abramov A, Franco L, Puiggali J, Enshaei H, Aleman C, Ddiazaz DD. Thermoresponsive shape-memory hydrogel actuators made by phototriggered click chemistry. Adv Funct Mater 2020;30(24):2001683.
[37] Park JK, Eisenhaure JD, Kim S. Reversible underwater dry adhesion of a shape memory polymer. Adv Mater Interfaces 2019;6(3):1801542.
[38] Leverant CJ, Zhang YF, Cordoba MA, Leo SY, Charpota N, Taylor C, Jiang P. Macroporous superhydrophobic coatings with switchable wettability enabled by smart shape memory polymers. Adv Mater Interfaces 2021;8(13):2002111.
[39] Qi JX, Chen ZH, Jiang P, Hu WX, Wang YH, Zhao Z, Cao XF, Zhang SS, Tao R, Li Y, Fang DI. Recent progress in active mechanical metamaterials and construction principles. Adv Sci 2022;9(1):2102662.
[40] Basak S, Bandyopadhyay A. Solvent responsive shape memory polymers-evolution, current status, and future outlook. Macromol Chem Phys 2021;222(19):2100195.
[41] Li PC, Chen HY, Chiang KT, Yang H. Reversible embroidered ball-like antireflective structure arrays inspired by leafhopper wings. J Colloid Interface Sci 2021;599:119–29.
[42] Stöber W, Fink A, Bohn E. Controlled growth of monodisperse silica spheres in the micron size range. J Colloid Interface Sci 1968;26(1):62–9.
[43] Leverant CJ, Leo SY, Cordoba MA, Zhang YF, Charpota N, Taylor C, Jiang P. Reconfigurable anticounterfeiting coatings enabled by macroporous shape memory polymers. ACS Appl Polym Mater 2019;1(1):36–46.
[44] Leo SY, Zhang W, Zhang YF, Ni YL, Jiang H, Jones C, Jiang P, Basile V, Taylor C. Chromogenic photonic crystal sensors enabled by multistimuli-responsive shape memory polymers. Small 2018;14(12):1703515.
[45] Greg S, Sing K. Adsorption, surface area and porosity. New York: Academic Press; 1982.
[46] Ni YL, Zhang YF, Leo SY, Fang Y, Zhao MZ, Yu L, Schulze KD, Sawyer WG, Angelini TE, Jiang P, Taylor CR. Unconventional shape memory mechanisms of nanoporous polymer photonic crystals: implications for nano-optical coatings and devices. ACS Appl Nano Mater 2018;1(11):6081–90.
[47] Peng KY, Zhao Y, Shahab S, Mirzaeifar R. Ductile shape-memory polymer composite with enhanced shape recovery ability. ACS Appl Mater Interfaces 2020;12(52):58295–300.
[48] Dumlu H, Marquardt A, Zirdehi EM, Varnik F, Shen YC, Neuking K, Eggeler G. A mechanical analysis of chemically stimulated linear shape memory polymer actuation. Materials 2021;14(3):481.
[49] Zhu KK, Hu JL, Zhang LN. Editable and bidirectional shape memory chitin hydrogels based on physical/chemical crosslinking. Cellulose 2019;26(17):9085–94.